# Terra Rossa Genesis by Replacement of Limestone by Kaolinite. III. Dynamic Quantitative Model

*Amlan Banerjee*[1,*] *and Enrique Merino*[1,†]

*1. Department of Geological Sciences, Indiana University, Bloomington, Indiana 47405, U.S.A.*

**ABSTRACT**

We model quantitatively the chemical dynamics of terra rossa formation that we deduced earlier from new field and petrographic evidence. The key phenomenon is that authigenic kaolinite (a proxy for kaolinite solid solutions and other clays) replaces limestone at a downward-moving reaction front at the base of the existing terra rossa. The chemical elements needed to make the authigenic clay are assumed to come from dissolution of eolian clay dust deposited at the surface. The model consists of equations of mass conservation (in one spatial dimension) that incorporate infiltration, diffusion, and replacement and dissolution reactions. Distinctive elements of the model are that (1) the kinetics of the kaolinite-for-calcite replacement is dominated by the crystallization stress generated by the kaolinite growth, in accordance with the view that replacement happens not by dissolution-precipitation but by guest-mineral-growth-driven pressure solution of the host; (2) the field observation that the terra rossa–forming front is narrow indicates that the growth of kaolinite at the front proceeds roughly at the pace at which the appropriate aqueous reactants reach the front, which in turn warrants scaling time, length, and concentrations such that transport and reaction terms are of the same order of magnitude; and (3) the huge contrast between aqueous concentrations and mineral densities, in effect, makes the scaled equation of mass conservation steady state. Numerical simulations correctly reproduce the formation of two adjacent zones in the moving reaction front—replacement and leaching—and of considerable secondary porosity in the leaching zone. This leaching porosity maximum constitutes a solitary wave, or soliton, that moves with the front. The simulations produce a range of predicted front widths that bracket the observed front width. Similarly, model-predicted front velocities of a few meters per million years agree well, within an order of magnitude, with both (1) a paleomagnetically derived rate of terra rossa formation at Bloomington and (2) the rate of authigenic clay formation that could be expected to form—by clay dissolution at the surface, downward infiltration of aqueous solutes, and precipitation of new clay at the front—from average clay dust deposition rates as measured today.

**Online enhancements:** appendixes.

## Introduction

We proposed, in an earlier work, a new chemical-dynamical theory to account for the formation of terra rossa by replacement of the underlying limestone by authigenic red kaolinite and other clays (Merino and Banerjee 2008). The theory, summarized in the next section, was based on excellent petrographic evidence of clay-for-limestone replacement obtained on samples collected at the bottom of the terra rossa at Bloomington, Indiana. The microscopic evidence of volume-for-volume replacement agreed with macroscopic, paleomagnetic evidence of constant rock volume reported in Meert et al. (2009).

The purpose of this article, the last of the series, is to model the new terra rossa–forming process quantitatively and, in particular, to compare model-calculated rates of formation of terra rossa to rates obtained paleomagnetically (Meert et al. 2009).

Manuscript received November 18, 2009; accepted December 18, 2010.

* Author for correspondence; present address: Department of Earth and Environmental Science, New Mexico Institute of Mining and Technology, Socorro, New Mexico 87801, U.S.A.; e-mail: amlan@nmt.edu.

† E-mail: merino@indiana.edu.

[The Journal of Geology, 2011, volume 119, p. 259–274]  0022-1376/2011/11902-0002$15.00. DOI: 10.1086/659146

### Summary of the Qualitative Model

The qualitative model is described in detail in Merino and Banerjee (2008) and Meert et al. (2009). The new model of terra rossa genesis is shown in figure 1. The terra rossa clay grows authigenically at a narrow reaction front at the base of the terra rossa, where it replaces the underlying limestone. The front travels downward by virtue of the mineral reactions that take place in it. The reaction front (fig. 2*a*) is about 9 cm thick and consists of a porous, leached-limestone zone, A, and a replacement zone, B. Zone B is the region where the authigenic replacement of limestone by red clay was last in progress. The aqueous reactants needed to make the new clays reach the reaction front by infiltration from above; they are the aqueous Al, Si, and Fe produced at the current land surface by dissolution of eolian-dust clay particles by rain and soil water. (From Amram and Ganor's [2005] experiments, one can derive dissolution half-lives of tens of years for smectite dust particles of size 1–100 $\mu$m dissolved in pH 5 water, and of tens of months for 0.1-$\mu$m smectite particles.) As aqueous Al, Si, and Fe reach zone B, new clay (which, for simplicity, we represent as pure kaolinite) grows via

$$0.33Al^{3+} + 0.33SiO_2 + 0.83H_2O = [Al_2Si_2O_5(OH)_4]_{1/6} + H^+ \quad (1)$$

and simultaneously pressure-dissolves an equal volume (see "Kinetics of the Kaolinite-for-Calcite Replacement") of host calcite, according to

$$CaCO_3 + H^+ = Ca^{2+} + HCO_3^-, \quad (2)$$

leading to the local mass balance,

$$0.45CaCO_{3(calc)} + 0.33Al^{3+} + 0.33SiO_2 + 0.83H_2O = [Al_2Si_2O_5(OH)_4]_{1/6} + 0.45Ca^{2+} + 0.45HCO_3^- + 0.55H^+, \quad (3)$$

where the coefficient 0.45 before the calcite formula accounts for mineral volume conservation. For simplicity, the predominant aluminum and carbonate species were assumed to be $Al^{3+}$ and $HCO_3^-$, respectively (Merino and Banerjee 2008), an assumption that results in a moderate overestimate of the amount of $H^+$ released by reaction (3). The reason for choosing a formula for kaolinite one-sixth the size of the standard nine-oxygen formula will become apparent below. The $H^+$ released in zone B by the mass balance (eq. [3]) travels downflow and quickly dissolves out of pores in an adjacent slice of fresh limestone according to reaction (2), giving rise to the observed secondary pores that define zone A of the front (fig. 2*c*). Note that calcite

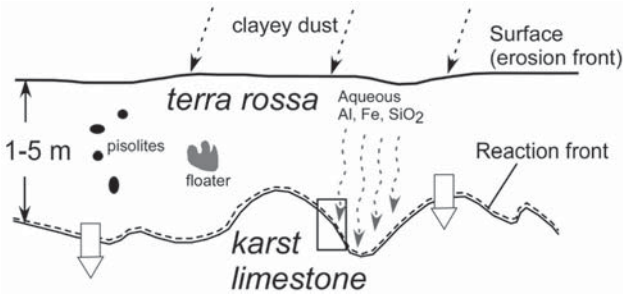


**Figure 1.** Schematic profile of a terra rossa claystone, with its associated underlying karst limestone. The terra rossa is bound by a thin reaction front at its bottom and the current erosion surface at its top. It contains iron oxide pisolites and in situ limestone "floaters," both excellent indicators of the authigenic origin of the terra rossa. The aqueous Al, Si, and Fe resulting from dissolution of eolian clay dust at the surface percolate down to the replacement front, driving growth of the authigenic clay in it. The approximate position of the reaction front shown in figure 2*a* is marked with a rectangle.

is dissolved simultaneously by two mechanisms: (1) in zone B, calcite is dissolved by pressure solution driven by kaolinite growth (as discussed in detail in "Kinetics of the Kaolinite-for-Calcite Replacement"), and (2) in zone A, calcite is dissolved chemically by the $H^+$ released by the mass balance equation (3) in zone B, at the same rate as these $H^+$ ions are released by equation (3). When zone B has been completely replaced, the replacement will start in what is now zone A, and the acid released will start dissolving pores in the calcite of a new zone A; this is how the front advances (downward in nature, fig. 1, and to the right in the sketch of fig. 4).

The actual kaolinite in terra rossa is red (and orange in thin section; see fig. 2) because it is $Fe^{3+}$ bearing, like that in laterites (Muller at al. 1995). Although the actual kaolinite is represented in the quantitative model below by pure kaolinite to keep the number of components and mass conservation equations to a minimum, it is simulated here by simply taking for it an equilibrium constant greater than that for pure kaolinite (see "Parameters Used").

In short, the chemical dissolution of calcite in zone A is coupled via the $H^+$ ions to the calcite pressure solution in zone B. This, in turn, is coupled via the crystallization stress to the growth of kaolinite, which is driven by the arrival at the front of aqueous Al, Si, and Fe, which are derived from dissolution of clay dust at the surface.

Meert et al. (2009) showed that the directions of

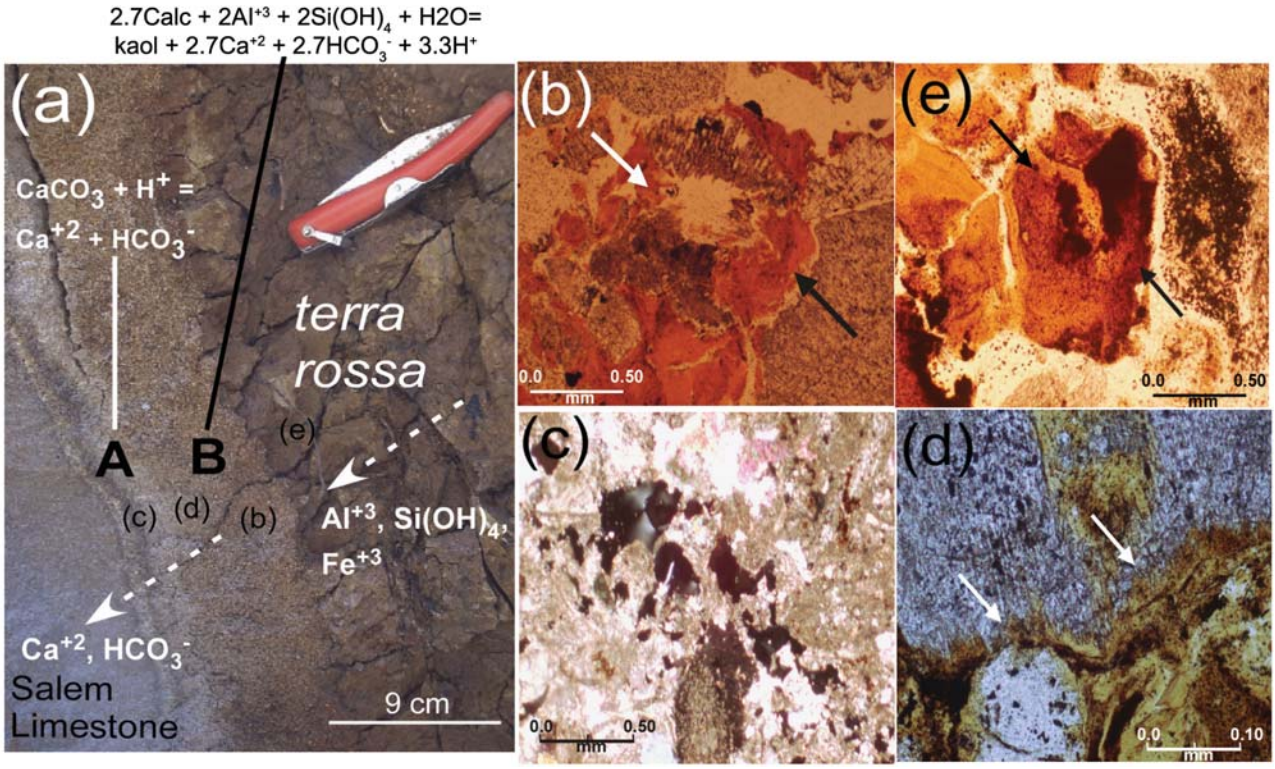


**Figure 2.** Summary of field and petrographic evidence, reproduced from Merino and Banerjee (2008). *a*, Reaction front between terra rossa and Salem Limestone on the Bloomington campus of Indiana University. The front consists of a bleached zone (*A*) ~3 cm wide and a replacement zone (*B*) ~6 cm wide. Approximate positions of the photomicrographs in *b*–*e* are marked. *b*, Crinoid columnal partly replaced by orange clay (at arrows) in the replacement zone (*B*). The circular shape of the replaced portions is preserved, indicating that the replacement was volume-for-volume, a fact used in adjusting the mass balance (eq. [3]). Plane-polarized light. *c*, Large secondary pores (areas in extinction) in the bleached zone (*A*). Crossed polars. *d*, Incipient replacement of a crinoid columnal by the orange clay (white arrows) in the replacement zone (*B*). Plane-polarized light. *e*, Crinoid columnal completely replaced by clay. The occurrence in the replacement zone of crinoid columnals in various stages of replacement by kaolinite, shown in *b*, *d*, and *e*, is additional evidence (beyond that described in Merino and Banerjee 2008) that the growth of kaolinite and the dissolution of calcite proceeded simultaneously and at the same rate.

remanent magnetism in a 1.8-m profile of terra rossa at Bloomington, Indiana, cluster closely around the earth's current magnetic-field direction, a fact that both points to in situ growth of the terra rossa clay (in agreement with the petrographic evidence of authigenesis) and indicates that its growth occurred within the past 0.78 m.yr., that is, since the earth's latest magnetic-field reversal, indicating a minimum terra rossa formation rate of 1.8/0.78 = 2 m/m.yr. Also, paleomagnetic directions obtained from unreplaced limestone "floaters" within the terra rossa are indistinguishable from directions in the bedrock limestone, indicating that the floaters preserve their original stratigraphic position. This, in turn, implies that the terra rossa under each floater occupies a volume equal to that of the limestone that has been replaced, which confirms macroscopically the microscopic evidence of volume conservation reported in Merino and Banerjee (2008).

We turn now to the kinetics of mineral replacement, especially applied to the kaolinite-for-calcite replacement of interest in our model.

## Kinetics of the Kaolinite-for-Calcite Replacement

In the preceding section, the kaolinite-for-calcite replacement was held to proceed not by dissolution-precipitation but by a kaolinite growth–driven pressure solution of the host limestone. This mechanism was explained in detail in "Replacement Physics" in Merino and Banerjee (2008, p. 68–69)

and references therein. Its great advantage over the idea of dissolution-precipitation is that it provides a strong, instantaneous coupling—the crystallization stress—between growth and dissolution, a coupling that automatically forces the growth of the guest and the dissolution of the host to proceed at the same rate, explaining why replacement preserves mineral volume. The demonstration that the crystallization stress automatically equalizes guest mineral growth and host mineral dissolution rates is reproduced from Nahon and Merino (1997) in figure 3*A* in a general case. The analogous plot in figure 3*B* shows the stress-coupled kinetics for the particular case of interest here, characterized by the fact that $k_{A(kaol)} \ll k_{B(calc)}$, which makes the kaolinite grow at practically its unconstrained rate and the calcite pressure-dissolve at that same very low rate, regardless of its own superhigh dissolution kinetics. This will be essential in "Quantitative Reaction-Transport Model" below.

Essentially, the replacement proceeds as follows. The guest mineral A, driven by supersaturation, starts to grow within the host rock B at its unconstrained rate $R^{growth}_{A,\,initial}$ and immediately starts to exert an induced stress, or crystallization stress, on the adjacent host as well as on itself. This stress increases the Gibbs free energies (Kamb 1961) and thus the equilibrium constants for both minerals, $K_A$ and $K_B$, simultaneously causing the A (guest) volumetric growth rate ($\approx k_A S_0^A[(Q_A/K_A) - 1]$) to decrease and the B (host) volumetric dissolution rate ($\approx k_B S_0^B[1 - (Q_B/K_B)]$) to increase until the two curves intersect. These trends are shown qualitatively in figure 3*A*. The point of intersection is at time $t^*$. From then on, the two volumetric rates remain equal to each other, explaining with generality why replacement automatically preserves mineral volume. However, for the kaolinite-for-calcite replacement of interest here, and because the rate constants of kaolinite and calcite differ by many orders of magnitude, with $k_{A(kaol)} \ll k_{B(calc)}$, the rate of replacement is practically equal to the unconstrained growth rate of kaolinite (see app. A, available in the online edition or from the *Journal of Geology* office),

$$R_{replacement} = k_A \ln \Omega_A = R_{unconstrained}, \qquad (4)$$

as shown in figure 3*B* by the practically horizontal kaolinite growth rate. This replacement kinetics will be used to advantage in our quantitative model of terra rossa formation below, "Quantitative Reaction-Transport Model," eliminating the need

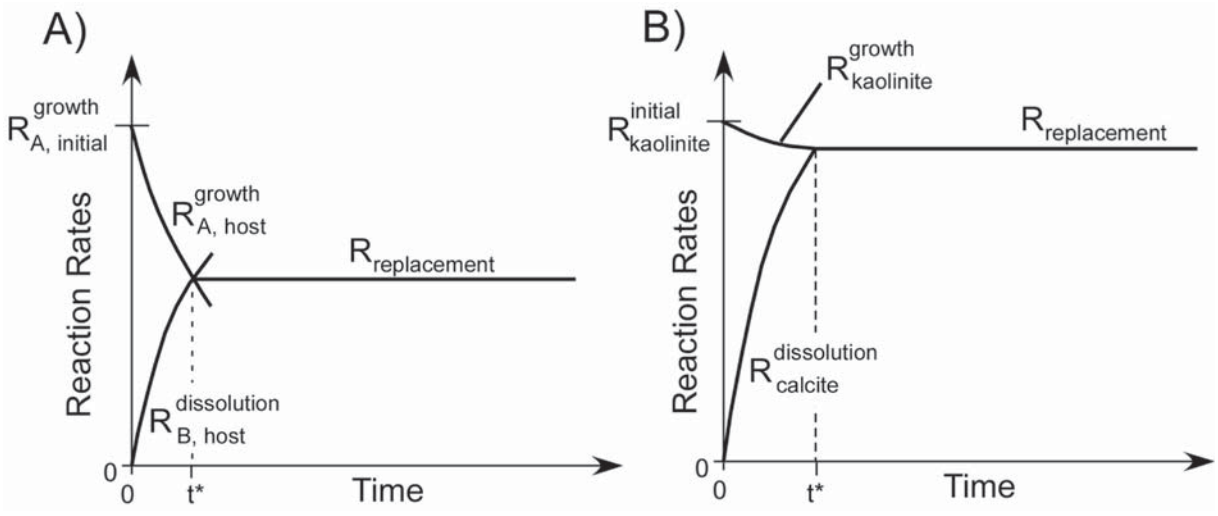


**Figure 3.** *A*, How guest-mineral growth automatically equalizes the volumetric rates of guest growth and host dissolution, explaining why replacement preserves mineral volume. See text, appendix A, available in the online edition or from the *Journal of Geology* office, and Nahon and Merino (1997). In the general case shown here, the guest and host minerals have rate constants not very different from each other, which causes the slopes of the two rate-versus-time curves to be steep. *B*, For the particular case of the kaolinite-for-calcite replacement, the kaolinite-growth branch is practically horizontal, whereas that for calcite dissolution is very steep, because $k_{kaol} \ll k_{calc}$; see appendix A. Consequently, the replacement rate is practically equal to the unconstrained initial growth rate of the kaolinite, a crucial factor for the quantitative model of "Quantitative Reaction-Transport Model."

to compute the crystallization stress. Nonetheless, the crystallization stress generated by the kaolinite growth and responsible for pressure-dissolving the calcite,

$$\text{stress}_{\text{xln}} = \frac{k_{\text{A}} \ln \Omega_{\text{A}}}{k_{\text{B}} V_0^{\text{B}}}, \tag{5}$$

turns out to be minute, because extremely little work is required for kaolinite to pressure-dissolve calcite (app. A; also figs. 3, 4 in Fletcher and Merino 2001).

## Quantitative Reaction-Transport Model

***Reaction-Transport Equations.*** The process of clay formation, its replacement of calcite, and the resulting leaching, as outlined above, can be described by a set of continuity reaction-transport equations for mass, together with mineral rate laws and initial and boundary conditions. For each relevant aqueous species $i$ in the system ($H^+$, $Al^{+3}$, $SiO_2$, $HCO_3^-$, and $Ca^{+2}$), the continuity equation is

$$\Gamma\phi \frac{\partial c_i}{\partial t} = \Gamma\phi D \frac{\partial^2 c_i}{\partial x^2} - \Gamma\phi U \frac{\partial c_i}{\partial x} + \sum_{j=1}^{2} \xi_{i,j} R_j. \tag{6}$$

Symbols are listed in table 1. The first two terms on the right represent the gradient of diffusive and advective fluxes, respectively. The last term represents the rates of production or consumption of aqueous species $i$ by each of the $j$ reactions in the front: $j = 1$, kaolinite growth in zone B (eq. [1]) and $j = 2$, chemical dissolution of calcite in zone A (eq. [2]). The factor $\Gamma = 10^{-3}$ L/cm$^3$ appears because we later use equilibrium constants consistent with mol/L but mineral reaction rates in mol/cm$^3$ s (Wang et al. 1995).

***Mineral Reaction Rates.*** For each reaction involved in the reaction front, we adopt a basic linear rate law whereby rate is proportional to the thermodynamic affinity (Aagaard and Helgeson 1982). For our reactions (1) and (2) the affinity is proportional to $RT\ln\Omega$, where the supersaturation is $\Omega = Q/K_{\text{eq}}$ and the ion activity product $Q$ is written in terms of all relevant aqueous concentrations

**Table 1.** Notation

| Symbol | Definition | Units |
|---|---|---|
| $c_i$ | Concentration of $i$th species | mol/L of pore volume |
| $C$ | Average concentration used as scale for concentrations | mol/L of pore volume |
| $c_i^{\text{ic}}$, $c_i^{\text{bc}}$ | Initial and boundary concentrations of species $i$ | mol/L of pore volume |
| $\gamma_i$ | Scaled concentration of species | Dimensionless |
| $t$ | Time | s |
| $T$ | Timescale | s |
| $\tau$ | Scaled time, defined as $t = T\tau$ | Dimensionless |
| $x$ | Length | cm |
| $X$ | Length scale | cm |
| $\lambda$ | Scaled length, defined as $x = X\lambda$ | Dimensionless |
| $R_j$ | Rate of reaction for reaction $j$ | mol/(bulk cm$^3$ s) |
| $r_j$ | Scaled rate of reaction for reaction $j$ | Dimensionless |
| $k_j$ | Rate constant for reaction $j$ | mol/cm$^2$ s |
| $\eta_{\text{kaol}}$ | Volumetric rate constant for kaolinite; eq. (14a) | mol/cm$^3$ s |
| $\beta_{\text{calc}}$ | Scaled rate constant for calcite; eq. (16a) | |
| $D$ | Average effective diffusion coefficient of aqueous species | cm$^2$/s |
| $U$ | Water velocity through pores | cm/s |
| $\phi$ | Porosity | (cm$^3$ of pore volume)/(cm$^3$ of bulk rock) |
| $\phi_\ell$ | Leaching porosity | (cm$^3$ of pore volume)/(cm$^3$ of bulk rock) |
| $\Gamma$ | A factor of $10^{-3}$ L/cm$^3$; see eq. (6) | |
| $\xi_{i,j}$ | Stoichiometric coefficient of species $i$ in $j$th reaction | |
| $S_0$ | Specific surface area of a mineral with volume fraction of 1 | cm$^2$/(bulk cm$^3$) |
| $f$ | Factor equal to 0 or 1, defined in eq. (7) | |
| $K_{\text{eq}}^j$ | Equilibrium constant for chemical reaction $j$ | |
| $\rho_i$ | Molar density of mineral $j$ | mol/cm$^3$of $j$ |
| $v_j$ | Volume fraction of mineral $j$ | cm$^3$ of mineral $j$/(bulk cm$^3$) |
| p, d | Superscripts denoting precipitation and dissolution, respectively | |
| $\theta$ | Quantity defined in eq. (30) | |
| $Q_{\text{A}}$, $Q_{\text{B}}$ | Ion activity products of guest mineral A and host mineral B, respectively | |

(taken as proxies for the activities), ensuring that all of them interact in the calculations.

*Kaolinite Growth in Zone B.* For kaolinite growth (reaction [1]) in zone B, the rate law adopted is

$$R^{\mathrm{p}}_{\mathrm{kaol}} = k_{\mathrm{kaol}} S_{0,\mathrm{kaol}} v_{\mathrm{kaol}} f \left[ \frac{(c_{\mathrm{Al}^{+3}})^{1/3} (c_{\mathrm{SiO_2}})^{1/3}}{c_{\mathrm{H}^+} K^{\mathrm{kaol}}_{\mathrm{eq}}} - 1 \right], \quad (7)$$

where $S_0$ is specific surface area of kaolinite, and $v$ is the kaolinite volume fraction (see app. B, available in the online edition or from the *Journal of Geology* office). The factor $f$ in the rate law ensures that kaolinite grows only where there is calcite to be replaced, that is, only at the reaction front. With $v_{\mathrm{calc}}$ denoting the volume fraction of calcite, if $v_{\mathrm{calc}} \leq 0.01$, then $f = 0.0$, that is, no kaolinite grows; if $v_{\mathrm{calc}} > 0.01$, then $f = 1.0$, that is, kaolinite may grow.

We assume that all activity coefficients are equal to 1, and we use molarity for molality units in all equations. Our choice of kaolinite formula ($[Al_2Si_2O_5(OH)_4]_{1/6}$) in reaction (1) makes the exponent on $c_{\mathrm{H}^+}$ in equation (7) unity. If we had chosen as the kaolinite formula the usual $Al_2Si_2O_5(OH)_4$, then the exponent on aluminum and silica concentrations would have been 2 in equation (7), and that on $c_{\mathrm{H}^+}$ would have been 6. This high exponent would exaggerate the effect of $c_{\mathrm{H}^+}$, and even very small changes in $c_{\mathrm{H}^+}$ would make the solution numerically unstable.

*Pressure Solution of Host Calcite in Zone B.* As explained in "Kinetics of the Kaolinite-for-Calcite Replacement" and in figure 3*B*, the pressure solution of calcite driven by the crystallization stress generated by kaolinite growth takes place not according to the conventional calcite rate law, but according to the volumetric, unconstrained growth rate of kaolinite, $R^{\mathrm{p}}_{\mathrm{kaol}}/\rho_{\mathrm{kaol}}$.

*Chemical Dissolution of Calcite in Zone A.* The rate law adopted for chemical dissolution of calcite (by the released $H^+$ during replacement in zone B; reaction [3]) in zone A is

$$R^{\mathrm{d}}_{\mathrm{calc}} = k_{\mathrm{calc}} S_{0,\mathrm{calc}} v_{\mathrm{calc}} a_{\mathrm{H}^+} \left( 1 - \frac{c_{\mathrm{Ca}^{+2}} c_{\mathrm{HCO_3^-}}}{c_{\mathrm{H}^+} K^{\mathrm{calc}}_{\mathrm{eq}}} \right). \quad (8)$$

This rate law includes calcite surface area (app. B), and it coincides with the first and last terms of the four-term rate law determined by Busenberg and Plummer (1986).

***Initial and Boundary Conditions.*** *Initial Conditions.* The concentrations of the five relevant aqueous species $Al^{+3}$, $SiO_2$, $Ca^{+2}$, $HCO_3^-$, and $H^+$ throughout the limestone are initially such that the pore fluid has a pH of 7.0 and is in equilibrium with both calcite and kaolinite.

*Boundary Condition at* $x = 0$. Through the left boundary, figure 4*a*, enters a weakly acid (pH 5) aqueous solution slightly supersaturated with respect to kaolinite ($\Omega_{\mathrm{kaol}} = 3.0$) and undersaturated with respect to calcite.

*Boundary Condition at* $x = +\infty$. On the right side we impose the condition that the gradient of all aqueous concentrations be 0, $\partial c_i/\partial x = 0$.

***Volume Change.*** As a result of chemical dissolution and pressure dissolution of calcite and precipitation of kaolinite, the volume fractions of these minerals change in time and space. The volumetric growth rate of kaolinite in zone B at any moment is given by

$$\frac{\partial v_{\mathrm{kaol}}}{\partial t} = \frac{R^{\mathrm{p}}_{\mathrm{kaol}}}{\rho_{\mathrm{kaol}}}. \quad (9)$$

The rate of volume change of calcite consists of two terms, calcite pressure-dissolved in zone B and calcite chemically dissolved in zone A:

$$\frac{\partial v_{\mathrm{calc}}}{\partial t} = -\left[ (1 - \phi_\ell) \frac{R^{\mathrm{p}}_{\mathrm{kaol}}}{\rho_{\mathrm{kaol}}} + \frac{R^{\mathrm{d}}_{\mathrm{calc}}}{\rho_{\mathrm{calc}}} \right]. \quad (10)$$

In addition, all volume fractions must satisfy the relation

$$v_{\mathrm{calc}} + v_{\mathrm{kaol}} + \phi_\ell = 1 - \phi, \quad (11)$$

where $\phi_\ell$ is the leaching porosity produced earlier by chemical dissolution of calcite and $\phi$ is the (assumed constant) rock porosity of both terra rossa and limestone outside the reaction front.

***Scaling of the Dynamic Equations.*** We now scale the system of equations (6)–(10), taking advantage of the fact that the reaction front is narrow (see fig. 2*a*), a feature of terra rossa formation that indicates that kaolinite grows and replaces calcite in the reaction zone B as fast as its aqueous ingredients are delivered to the front, which in turn implies that mineral growth rates and transport terms in equation (4) should have the same order of magnitude. This kind of self-consistent scaling was also carried out by Wang et al. (1995) and Ortoleva et al. (1982, p. 625–627) in models of lateritic weathering and metamorphic layering, respectively. Here, it consists of the following steps.

*1. Dimensionless, Order-One Variables.* We define new scaled parameters for time ($\tau$), length ($\lambda$), and concentration ($\gamma$) that are dimensionless and of order unity, according to

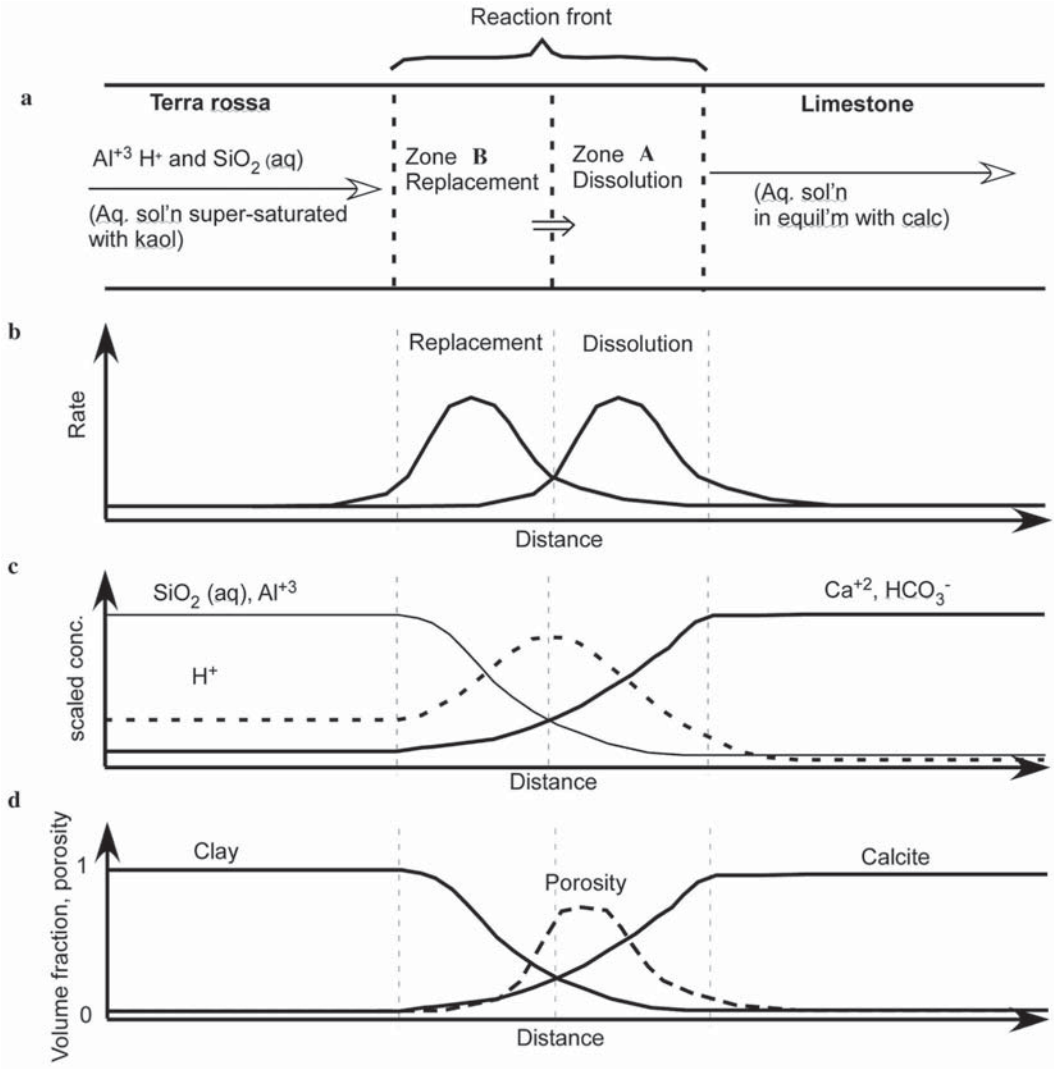


**Figure 4.** Model system and expected qualitative profiles of mineral modes and aqueous species across the replacement zone (*B*) and the leaching zone (*A*) of figure 2*b*. *a*, With supply of aqueous $Al^{+3}$ and $SiO_2$ from the left, kaolinite grows and partly replaces calcite in zone B. This replacement releases $H^+$ (eq. [1]), which quickly dissolves more limestone by reaction (3), generating pores (fig. 2*c*) in the bleached zone A. *b*, Expected profile of the reaction rates of replacement and dissolution in the front. The two rates are coupled via $H^+$. *c*, Expected profile of aqueous-species concentrations across the system. $Al^{+3}$ and $SiO_2$ are consumed in the replacement zone, while $H^+$ is produced there and is immediately consumed by dissolving limestone in the leaching zone. *d*, Schematic profiles of clay, calcite, and secondary porosity at an intermediate position of the front.

$$\tau = \frac{t}{T}, \qquad \lambda = \frac{x}{X}, \qquad \gamma_i = \frac{c_i}{C}; \tag{12}$$

the scales $T$, $X$, and $C$ are determined below.

*2. Scaling Mineral Rates.* For kaolinite precipitation in zone B, by inserting $C\gamma_i = c_i$ into equation (7) we obtain

$$R^{\mathrm{p}}_{\mathrm{kaol}} = \eta_{\mathrm{kaol}} r^{\mathrm{p}}_{\mathrm{kaol}}, \tag{13}$$

where

$$\eta_{\mathrm{kaol}} = k_{\mathrm{kaol}} S_{0,\,\mathrm{kaol}} \tag{14a}$$

and

$$r^{p}_{kaol} = v_{kaol} f\left(\frac{\gamma^{1/3}_{Al^{+3}}\gamma^{1/3}_{SiO_2}}{C^{1/3}\gamma_{H^+}K^{kaol}_{eq}} - 1\right). \quad (14b)$$

Here, $\eta_{kaol}$ is the new rate constant (one that incorporates the specific grain surface and is in units of mol/cm$^3$ s), and $r^{p}_{kaol}$ is the scaled kaolinite growth rate of order 1.

Similarly, for the calcite chemical dissolution in zone A, the rate law, equation (8), becomes

$$R^{d}_{calc} = \eta_{kaol}\beta_{calc} r^{d}_{calc}, \quad (15)$$

where

$$\beta_{calc} = \frac{Ck_{calc}}{k_{kaol}}, \quad (16a)$$

$$\eta_{kaol} = k_{kaol}S_0, \quad (16b)$$

and

$$r^{d}_{calc} = \gamma_{H^+}V_{calc}\left(1 - \frac{C\gamma_{Ca^{+2}}\gamma_{HCO_3^-}}{\gamma_{H^+}K^{calc}_{eq}}\right). \quad (16c)$$

Dividing equation (15) by equation (13), we obtain

$$\frac{R^{d}_{calc}}{R^{p}_{kaol}} = \beta_{calc}\frac{r^{d}_{calc}}{r^{p}_{kaol}} = \beta_{calc}, \quad (17)$$

because both $r^{p}_{kaol}$ and $r^{d}_{calc}$ are of order 1. With values of $C$, $k_{kaol}$, and $k_{calc}$ from table 2, we obtain

$$\beta_{calc} = 10^7. \quad (18)$$

This expresses the fact that the chemical dissolution of calcite—if uncoupled—is seven orders of magnitude faster than the growth of kaolinite. However, in our case, the chemical dissolution of calcite effected in zone A is coupled to, and therefore cannot be faster than, the rate of release of $H^+$ ions by replacement in zone B. This coupling requires that in our model, regardless of the huge value of $\beta_{calc}$ in equation (18), we must set

$$\beta_{calc} = 1. \quad (19)$$

*3. Scaling Time on Kaolinite Growth.* The rate of volume fraction change of kaolinite, from equations (9), (12), and (13), is

$$\frac{\partial V_{kaol}}{\partial \tau} = \left(\frac{T\eta_{kaol}}{\rho_{kaol}}\right) r^{p}_{kaol}. \quad (20)$$

We tie the timescale on kaolinite growth, the driving reaction, by simply setting the right side of equation (18) to be of order 1. Because the left side of equation (18) and $r^{p}_{kaol}$ are already of order 1, it follows that

$$\frac{T\eta_{kaol}}{\rho_{kaol}} = 1, \quad (21)$$

from which

$$T = \frac{\rho_{kaol}}{\eta_{kaol}}. \quad (22)$$

**Table 2.** Typical Ranges of Values Adopted in Numerical Simulations

| Variable | Symbol | Values adopted |
|---|---|---|
| Concentration scale | $C$ | $10^{-5}$ mol/L |
| Diffusion coefficient | $D$ | $10^{-5}$ cm$^2$/s |
| Annual rainfall | RF | 2–0.5 m/yr |
| Porosity | $\phi$ | 0.01–0.1 |
| Velocity of water[a] | $U$ | $1.6 \times 10^{-5}$ to $4 \times 10^{-6}$ cm/s |
| Grain size | $L$ | 0.1–1 mm |
| Specific surface area | $S_0$ | 600–60 cm$^{-1}$ |
| Factor (see eq. [4]) | $\Gamma$ | $10^{-3}$ L/cm$^3$ |
| Equilibrium constant, kaolinite[b] | $K_{eq,\ kaol}$ | 17.1, 54.1, 100 |
| Equilibrium constant, calcite | $K_{eq,\ calc}$ | 51.3 |
| Rate constant, kaolinite[b] | $k_{kaol}$ | $5 \times 10^{-15}$ to $6 \times 10^{-17}$ mol/cm$^2$ s |
| Rate constant, calcite | $k_{calc}$ | $10^{-5}$ mol/cm$^2$ s |
| Scaled rate constant, equation (16c)[c] | $\beta_{calc}$ | 1.0 |
| Kaolinite molar density[b] | $\rho_{kaol}$ | 0.06 mol/cm$^3$ |
| Calcite molar density | $\rho_{calc}$ | 0.027 mol/cm$^3$ |
| Supersaturation with kaolinite | $\Omega_{kaol}$ | 3 (boundary condition) |
| Initial kaolinite modal abundances | | 0.01–0.1 |
| Initial calcite modal abundances | | 0.98–0.8 |

[a] We set rainfall in the Bloomington area between 2 and 0.5 m/yr. We assume that only 25% of it infiltrates and divide it by the porosity (0.01–0.1) to obtain water velocity $U$ within terra rossa and limestone.

[b] Values refer to a kaolinite formula one-sixth the size of its usual formula, $Al_2Si_2O_5(OH)_4$.

[c] Where $\beta_{calc} = Ck_{calc}/k_{kaol}$. This scaled rate constant is $10^7$ for uncoupled dissolution of calcite. But dissolution of calcite in leaching zone A is coupled to release of $H^+$ ions by the replacement reaction (1) in zone B; thus, $\beta_{calc}$ must be set to 1 to keep the chemical leaching of calcite of the same order of magnitude as the kaolinite-for-calcite replacement.

This defines the timescale $T$. Depending on values chosen in this article for the kaolinite rate constant and the specific surface area, $T$ is of the order of $10^3$–$10^5$ yr. Equation (20) becomes

$$\frac{\partial V_{\text{kaol}}}{\partial \tau} = r^{\text{p}}_{\text{kaol}}, \tag{23}$$

and equation (10) becomes

$$\frac{\partial V_{\text{calc}}}{\partial \tau} = -\left[(1-\phi_\ell) r^{\text{p}}_{\text{kaol}} + \frac{\rho_{\text{kaol}}}{\rho_{\text{calc}}} r^{\text{d}}_{\text{calc}}\right]. \tag{24}$$

*4. Scaling the Continuity Equation.* We introduce the scaled variables in the continuity equation (eq. [6]),

$$\frac{\Gamma\phi C}{T}\frac{\partial \gamma_i}{\partial \tau} = \frac{\Gamma\phi DC}{X^2}\frac{\partial^2 \gamma_i}{\partial \lambda^2} - \frac{\Gamma\phi UC}{X}\frac{\partial \gamma_i}{\partial \lambda} + \eta_{\text{kaol}} \sum_{j=1}^{2} \xi_{i,j} r_j, \tag{25}$$

replace $T$ with $\rho_{\text{kaol}}/\eta_{\text{kaol}}$ in equation (25), and divide by $\eta_{\text{kaol}}$ to leave the reaction term of order 1:

$$\frac{\Gamma\phi C}{\rho_{\text{kaol}}}\frac{\partial \gamma_i}{\partial \tau} = \frac{\Gamma\phi DC}{\eta_{\text{kaol}} X^2}\frac{\partial^2 \gamma_i}{\partial \lambda^2} - \frac{\Gamma\phi UC}{\eta_{\text{kaol}} X}\frac{\partial \gamma_i}{\partial \lambda} + \sum_{j=1}^{2} \xi_{i,j} r_j. \tag{26}$$

*5. Making Transport and Reaction of the Same Order of Magnitude.* Since the reaction term and all the derivatives in equation (26) are now of order 1, we can impose the condition that kaolinite growth must be as fast as transport of aqueous species by making the coefficient of the diffusion term also of order 1,

$$\frac{\Gamma\phi DC}{\eta_{\text{kaol}} X^2} = 1. \tag{27}$$

This relationship connects the concentration ($C$) and length scales ($X$) as follows.

*6. Concentration and Length Scales.* The choice in equation (18) tied the timescale $T$ to kaolinite growth and led to equation (19). We now take $C = 10^{-5}$ mol/L, a probably typical order of magnitude of aqueous concentrations in our model, where the relevant species $Ca^{2+}$, $HCO_3^-$, $Al^{3+}$, $SiO_2$, and $H^+$ are expected to be between $10^{-4}$ and $10^{-6}$ mol/L. The third choice was equation (27), which yields the self-consistent value of the length scale $X$,

$$X = \left(\frac{\Gamma\phi DC}{\eta_{\text{kaol}}}\right)^{0.5} = \left(\frac{\Gamma\phi DC}{k^{\text{p}}_{\text{kaol}} S_0}\right)^{0.5}. \tag{28}$$

The scales $T$, $C$, and $X$ are now defined. See tables 2, D1, and D2 (the latter two available in the online edition or from the *Journal of Geology* office). Putting the scaled variables and scaling choices into place, equation (26) reduces to

$$\frac{\Gamma\phi C}{\rho_{\text{kaol}}}\frac{\partial \gamma_i}{\partial \tau} = \frac{\partial^2 \gamma_i}{\partial \lambda^2} - \theta\frac{\partial \gamma_i}{\partial \lambda} + \sum_{j=1}^{2} \xi_{i,j} r_j, \tag{29}$$

where

$$\frac{\Gamma\phi UC}{\eta_{\text{kaol}} X} = \theta. \tag{30}$$

*7. Natural Scaling.* Finally, as pointed out by Ortoleva et al. (1987) and Wang et al. (1995), the coefficient of the $\partial\gamma_i/\partial\tau$ term on the left side of equation (29) is always very small because of the inherently huge difference between typical aqueous concentrations and mineral densities, especially in low-temperature environments. With values from table 2 and the choice of $10^{-5}$ mol/L as the concentration scale $C$, the coefficient $(\Gamma\phi C/\rho_{\text{kaol}})$ is in our case between $10^{-8}$ and $10^{-9}$. This indeed makes the left side of equation (29) vanish, leaving

$$\frac{\partial^2 \gamma_i}{\partial \lambda^2} - \theta\frac{\partial \gamma_i}{\partial \lambda} + \sum_{j=1}^{2} \xi_{i,j} r_j = 0, \tag{31}$$

where $i$ is $H^+$, $Al^{+3}$, $SiO_2$, $HCO_3^-$, or $Ca^{+2}$. Note that the self-consistent scaling results in a differential equation of mass conservation with only one parameter, $\theta$, given by equation (30), which combines many of the relevant individual parameters of the terra rossa–forming process (infiltration velocity, porosity, concentration length scales, and timescales).

## Numerical Simulations

The scaled system of equations (eqq. [14b], [16c], [23], [24], and [31]) has been solved numerically for 24 sets of values of the relevant parameters, listed in tables 3, D1, and D2. The calculation scheme is given in appendix C, available in the online edition or from the *Journal of Geology* office.

***Parameters Used.*** Many parameters enter into each simulation: infiltration velocity, limestone and terra rossa porosity, kaolinite specific surface area, kaolinite rate constant, equilibrium constant, supersaturation of the aqueous solution reaching the front with respect to kaolinite, initial and boundary conditions imposed, etc. Each parameter has been given values within a certain range, as discussed next. All parameter values for each numerical run are listed in tables D1 and D2.

The kaolinite equilibrium constant, $K_{\text{eq}}$, was given values ranging from that for pure kaolinite upward. This assumes that the equilibrium constant for $Fe^{3+}$-bearing kaolinite solid solutions—which are the clays actually making up terra

**Table 3.** Initial and Boundary Conditions Adopted for the Base Run

| | Chosen (mol/L) | Scaled |
|---|---|---|
| Initial concentrations: | | |
| $Al^{+3}$ | $10^{-9}$ | $10^{-4}$ |
| $H^{+}$ (pH) | $1.66 \times 10^{-7}$ (6.78) | $1.66 \times 10^{-2}$ |
| $SiO_2$ | $1.6 \times 10^{-8}$ | $1.6 \times 10^{-3}$ |
| $Ca^{+2}$ | $5.41 \times 10^{-3}$ | $5.41 \times 10^{2}$ |
| $HCO_3^-$ | $1.64 \times 10^{-3}$ | $1.64 \times 10^{2}$ |
| Boundary concentrations, left side:[a] | | |
| $Al^{+3}$ | $10^{-5}$ | 1 |
| $H^{+}$ (pH) | $10^{-5}$ (5) | |
| $SiO_2$ | $10^{-5}$ | 1 |
| $Ca^{+2}$ | $5.41 \times 10^{-5}$ | 5.41 |
| $HCO_3^-$ | $3 \times 10^{-5}$ | 3.0 |

Note. Scaled values refer to a concentration scale of $C = 10^{-5}$ mol/L.

[a] Concentration of the aqueous species in the water entering the limestone model system.

rossa—is greater than that for pure kaolinite, an assumption consistent with previous work on the stability of phyllosilicate solid solutions (Merino 1975; Merino and Ransom 1982; Vieillard 2000). The $K_{eq}$ value for pure kaolinite, $Al_2Si_2O_5(OH)_4$, namely, $10^{7.4}$, was taken from Bowers et al. (1984). The equilibrium constant for the pure "one-sixth kaolinite," $[Al_2Si_2O_5(OH)_4]_{1/6}$, adopted in this article thus becomes $10^{(7.4/6)}$ (=17). For the more realistic kaolinite solid solutions in some of the runs in tables D1 and D2, $K_{eq} = 54$ and 100.

The volumetric rate constant for kaolinite, $\eta_{kaol}$ (see fig. 6 and tables D1 and D2), was assigned values ranging from $10^{-15}$ mol one-sixth kaolinite/cm$^3$ s for pure kaolinite to an assumed $10^{-12}$ mol one-sixth kaolinite (solid solution)/cm$^3$ s for the more realistic red clay minerals, in particular kaolinite solid solutions, that make up terra rossa. The values of $k_{kaol}$ used cover the range from $6 \times 10^{-17}$ mol/cm$^2$ s for pure one-sixth kaolinite (estimated from published data; see table 4 and its footnote) upward. The values of $S_0$ used cover one order of magnitude, from 600 to 60 cm$^{-1}$, according to grain size; see appendix B and tables D1 and D2. The rock porosity, $\phi$, of both limestone and terra rossa was set in the simulations as either 0.01, which is very low, or 0.1, which is moderate.

Adopted values of infiltration velocity, diffusion coefficient, clay grain size, clay molar density, supersaturation with kaolinite, and initial kaolinite and calcite modal abundances are given in table 2. The infiltration velocity was assumed to result from one-tenth of rainfall divided by rock porosity, with rainfall ranging from 2 to 0.5 m/yr. The boundary-condition supersaturation with clay was only 3 for all 24 runs in tables D1 and D2, and values of up to 10 were used for the runs carried out to assess sensitivity (see "Sensitivity of Model Predictions").

***Numerical Simulations.*** Twenty-four numerical simulations were carried out with the scaled system of equations (eqq. [14b], [16c], [23], [24], and [31]), each for a set of relevant parameter values listed in tables D1 and D2. For each simulation, the time and length scales $T$ and $X$, calculated from equations (22) and (28), respectively, and the calculated front thickness and front velocity are given in tables D1 and D2. The latter two quantities are also plotted in figure 6 versus $K_{eq}$ and $\eta_{kaol}$ for two porosities, 0.1 and 0.01, and are compared to field observations.

The evolution of several calculated quantities versus scaled space and time is shown graphically for run 6 in figure 5. The quantities shown are volume fraction of clay and calcite (fig. 5*A*), scaled replacement rate in zone B and dissolution rate in zone A (fig. 5*B*), saturation states for clay and calcite (fig. 5*C*), and dissolution porosity and pH (fig. 5*D*). Each frame contains two sets of curves: the thin curves correspond to a duration of 2 scaled time units, and the thick curves correspond to a duration of 4 scaled time units.

Each run has its own set of time and length scales resulting from the self-consistent scaling. For run 6, the time and length scales are $T = 6600$ yr and $X = 0.42$ cm, respectively. In equation (22), we see that the timescale depends simply on the clay's volumetric rate constant, $\eta_{kaol}$. Since, as mentioned

**Table 4.** Reported Rates of Kaolinite Growth or Dissolution

| Rate (mol/m$^2$ s) | pH | References |
|---|---|---|
| $10^{-13}$ to $4 \times 10^{-13}$ | 3 | Metz and Ganor 2001 |
| $1.5 \times 10^{-13}$ to $2 \times 10^{-13}$ | 3 | Carroll-Webb and Walther 1988 |
| $7.5 \times 10^{-13}$ | 3 | Wieland and Stumm 1992 |
| $7 \times 10^{-13}$ to $8 \times 10^{-13}$ | 3 | Ganor et al. 1995 |
| $1.24 \times 10^{-12}$ | 3 | Nagy et al. 1991 |

Note. From these measured rates, we deduce a rate constant of $\sim 10^{-17}$ mol $(Al_2Si_2O_5(OH)_4$/cm$^2$ s for kaolinite, equivalent to $6 \times 10^{-17}$ mol $[(Al_2Si_2O_5(OH)_4]_{1/6}$/cm$^2$ s and consistent with the rate law in equation (7). For $Fe^{+3}$-bearing kaolinite solid solution, we increase the rate constant to $10^{-16}$ and $10^{-15}$ in the numerical simulations (see text).

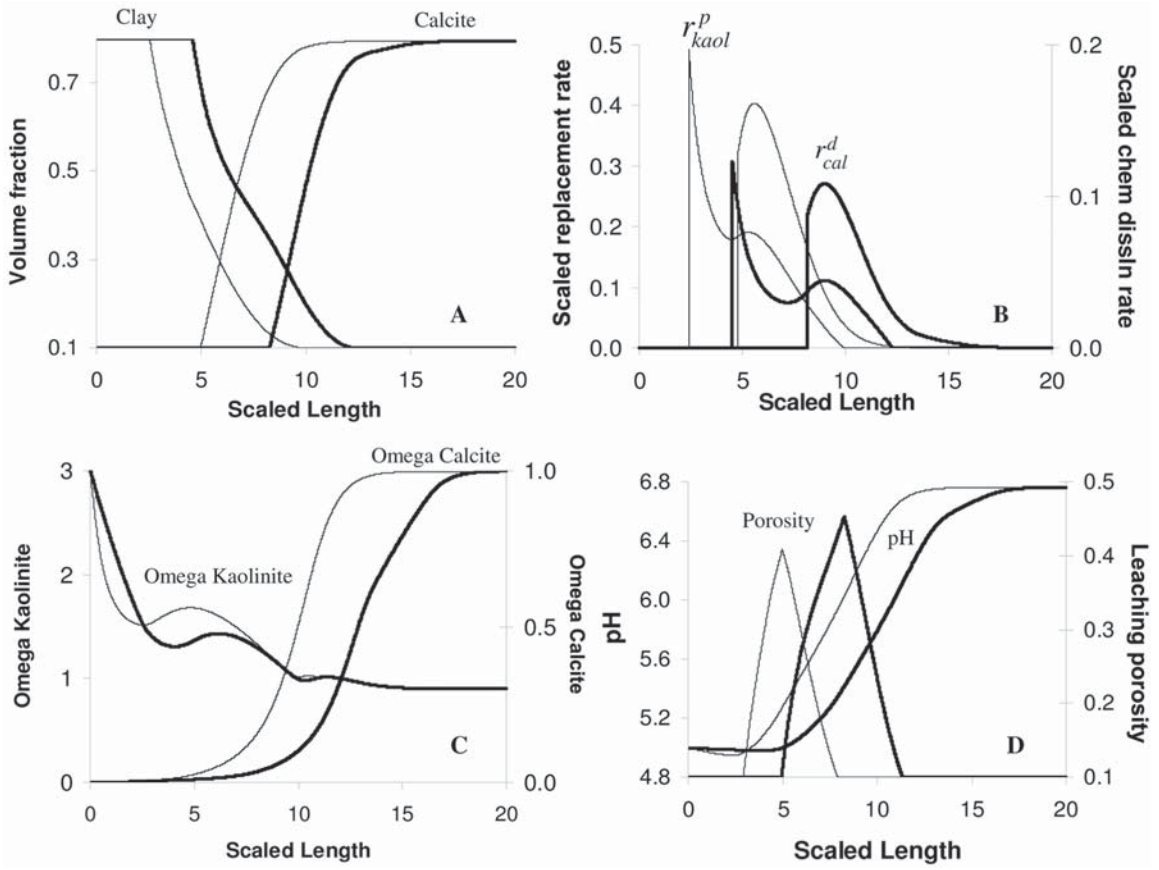


**Figure 5.** Numerical results for run 6, table D1, available in the online edition or from the *Journal of Geology* office, shown as functions of scaled distance and for two scaled times, $\tau = 2.0$ (13,200 yr; *thin lines*) and $\tau = 4.0$ (26,400 yr; *thick lines*). Simulation parameters include a high kaolinite rate constant and high rock porosity. Time and length scales for this run are 6600 yr and 0.42 cm. The front velocity calculated from the profiles is about 4 scaled length units per 2 scaled time units, or 1.7 cm/13,200 yr (1.2 m/m.yr.), in good agreement with the minimum rate of 2 m/m.yr. derived by Meert et al. (2009) from paleomagnetic work summarized in "Summary of the Qualitative Model." The front width predicted from these profiles is 6 scaled length units, or ~3 cm, in good order-of-magnitude agreement with the observed 9 cm of figure 2*a*. See "Discussion and Conclusions."

above, $\eta_{\text{kaol}}$ is assigned values that span three orders of magnitude, the model-predicted timescales of the terra rossa–forming process for the 24 runs (tables D1, D2) also span three orders of magnitude, from 700 to 528,000 yr.

The timescale of each run is critical in computing the clay formation rate, or front velocity, predicted by the run. For run 6, we see from the profiles of figure 5 that the clay-forming front advances about 4 scaled length units (equivalent to 4 × 0.42 cm, or 1.7 cm) in 2 scaled time units (equivalent to 2 × 6600 = 13,200 yr). Thus, the front velocity calculated for run 6 is 1.7 cm/13,200 yr, or 1.2 m/m.yr., the value given in table D1. All the front velocities calculated in this way, one per run, are shown in the top frames of figure 6, and they are compared to independent estimates below.

The front thickness predicted in run 6 can be estimated visually from any of the panels of figure 5, especially figure 5*B*, where we see that the total width of zones B and A is about 10 scaled length units, which yields a front of 10 × 0.42 = 4.2 cm, the value given in the last row of table D1.

***Comparing Predictions to Observations.*** As expected, all the simulations carried out in this study reproduced correctly several qualitative spatial attributes observed in field (fig. 2*a*), namely, a reaction front consisting of two adjacent zones—replacement (zone B) and leaching (zone A)—in the correct sequence (fig. 5*B*), with clay-for-calcite replacement in the replacement zone and high dissolution porosity in the leaching zone. A more stringent test involves comparing the numerical simulations for front thickness and front velocity to independent values.

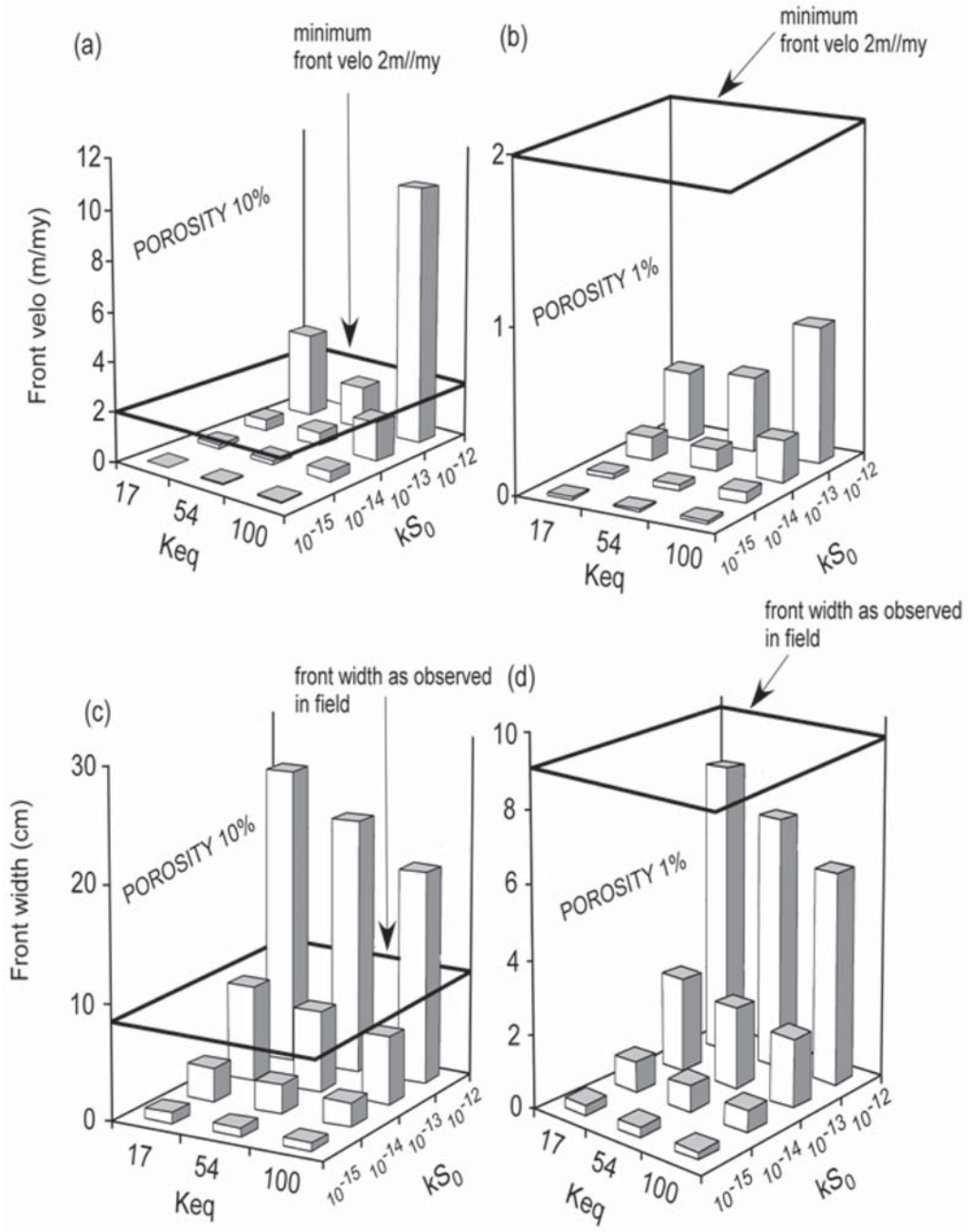


**Figure 6.** Predicted front velocity, or rate of terra rossa formation, in meters per million years (*top*) and front width in centimeters (*bottom*) of a clay-making front for a series of volumetric rate constants ($kS_0$) of kaolinite ranging from $10^{-15}$ mol/cm$^3$ s (equivalent to $k = 6 \times 10^{-17}$ mol/cm$^2$ s, referred to "one-sixth kaolinite") to $10^{-12}$ mol/cm$^3$ s (equivalent to $6 \times 10^{-15}$ mol/cm$^2$/s), kaolinite equilibrium constants ranging from 17 (referred to pure "one-sixth kaolinite") to 100, and porosity of both terra rossa and limestone (10% and 1%). Predictions for aqueous concentrations, clay and limestone volume fractions, and leaching porosity are not shown; they have the general trends shown for run 6 in figure 5. The front width of 9 cm observed in Bloomington (fig. 2*a*) is shown (*plane* in *c* and *d*) for comparison. The paleomagnetically derived minimum front velocity of 2 m/m.yr. is also shown for comparison (*plane* in *a* and *b*). Simulation parameters for each run are given in tables D1 and D2, available in the online edition or from the *Journal of Geology* office. In general, for a given rate constant, front velocity decreases but front width increases with increasing equilibrium constant. On the other hand, for a given equilibrium constant, an increase in the rate constant increases both front width and front velocity. The simulations show that for greater porosity (10%), the predicted front width (*c*) and front velocity (*a*) bracket the observed values fairly well.

For the front thickness, we see in figure 6*c* and 6*d* that the predicted values that best approximate the observed front thickness of 9 cm, which is marked in figure 6 by a horizontal rectangle, are those calculated for a fairly high volumetric rate constant of about $10^{-13}$ mol one-sixth kaolinite/cm$^2$ s at a moderate porosity of 0.1 (fig. 6*c*) and for a high rate constant of about $10^{-12}$ mol one-sixth kaolinite/cm$^2$ s at a low porosity of 0.01 (fig. 6*d*). It is clear in figure 6 that for the volumetric rate constant of pure kaolinite, about $10^{-15}$ mol one-sixth kaolinite/cm$^2$ s, the predicted front thickness is more than an order of magnitude lower than the observed 9 cm. This is consistent with the fact that the actual clay that always forms in terra rossa is never pure kaolinite but consists of red kaolinite (and other red clays) that contains considerable amounts of Fe and other cations, which, we estimated above, are responsible for its higher rate constant.

Finally, we compare the calculated front velocity, plotted vertically for the 24 runs in figures 6*a* and 6*b*, against two independent estimates: that obtained from paleomagnetic measurements in Meert et al. (2009) and that obtained from reasonable clay dust deposition rates.

1. As explained in "Summary of the Qualitative Model," paleomagnetic directions of terra rossa samples covering 1.8 m coincided with the current north, implying that they crystallized in less than 0.78 m.yr. (i.e., since the date of latest reversal) and thus that the minimum rate of authigenic terra rossa formation is 2 m/m.yr. This value is marked with a horizontal rectangle in figures 6*a* and 6*b*, which shows that only the front velocity simulations for moderate porosity (0.1) and highest volumetric rate constant used (~$10^{-12}$ mol one-sixth kaolinite/cm$^2$ s) can be commensurate with, or greater than, the "paleomagnetic" minimum of 2 m/m.yr. (see fig. 6*a*). This is consistent with the estimate we made earlier that the actual red kaolinite solid solution that mostly makes up terra rossa is bound to have a much higher rate constant than does pure kaolinite.

2. If, as proposed by Merino and Banerjee (2008), terra rossa is the authigenic equivalent of the eolian clay dust settled at a site, according to figure 1, then its formation rate should be roughly equivalent to the deposition rate of clay dust. An average supply of 10 g eolian clay dust/m$^2$ yr—about one-half of the total dust deposition rates measured by Smith et al. (1970), Rabenhorst et al. (1984), and Reheis and Rademaekers (1997)—would yield (by dissolution at the land surface, downward infiltration, and precipitation as new clay at the reaction front) an average of 5 mm of terra rossa (of assumed density 2 g/cm$^3$) per 1000 yr, or 5 m/m.yr., in rough agreement with the minimum value obtained paleomagnetically for Bloomington.

In summary, rates of terra rossa formation, or front velocities, predicted by the reaction-transport calculations for high clay volumetric rate constants and moderate porosity agree well within one order of magnitude with the two independent estimates discussed above, which agree with each other. Similarly, the front thicknesses predicted by the model for runs using high rate constants and moderate porosity come out equal to 10–20 cm, in good agreement with the value observed in the field (fig. 2*a*). These agreements between predicted and observed values appear to support the qualitative new theory of terra rossa formation proposed in Merino and Banerjee (2008).

***Sensitivity of Model Predictions.*** The sensitivity of the calculated front velocity and front thickness to porosity, clay equilibrium constant $K_{eq}$, and volumetric clay rate constant $\eta_{kaol}$ can be assessed from the top and bottom panels of figure 6, respectively. It is apparent in these figures that sensitivity to the clay equilibrium constant is low and that sensitivity to the porosity is low or moderate but that (because of eq. [19]) sensitivity is high to the volumetric rate constant $\eta_{kaol}$ ($=k_{kaol}S_{0,kaol}$), neither of whose factors, conventional rate constant and specific surface area, is well known. For the specific surface area, we have used the grain size dependence described in appendix C.

An additional 20 numerical simulations were carried out specifically to assess how sensitive the calculated front velocity and front thickness are to aqueous-ion diffusivity, boundary supersaturation with respect to kaolinite, clay grain size, and boundary pH of the clay-forming aqueous solution. The results are summarized in figure 7. It is apparent that the influence of boundary pH is negligible between pH 5 and 6 but considerable between pH 5 and 4 and that the influence of both diffusivity and supersaturation with kaolinite is minor.

## Discussion and Conclusions

***Geochemical Modeling and Petrography.*** The reaction-transport model of "Quantitative Reaction-Transport Model" and "Numerical Simulations" tests quantitatively the chemical dynamics of terra rossa formation proposed in Merino and Banerjee (2008), a dynamics driven by kaolinite growth. The model incorporates some field and petrographic observations and produces predictions that are compared to other observations not introduced in the model. Both the microscopic (petro-

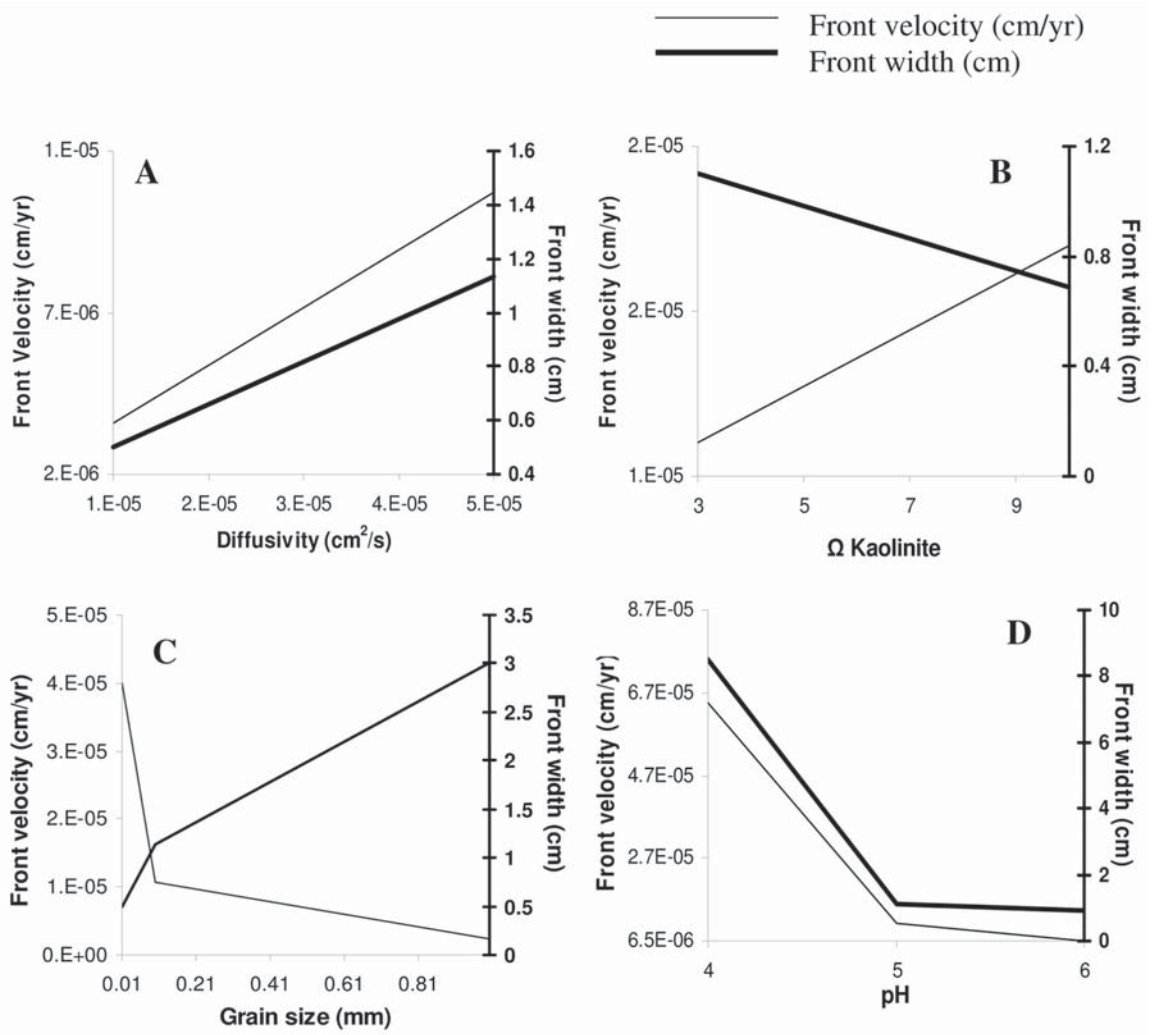


**Figure 7.** Sensitivity of front velocity (*thin lines*) and front thickness (*thick lines*) predicted for the base run to variations in input diffusivity (*A*), supersaturation with kaolinite (*B*), grain size (*C*), and input pH (*D*). *A*, Increase in the diffusivity of the aqueous species from $10^{-5}$ to $5 \times 10^{-5}$ cm$^2$/s causes both front velocity (*thin line*) and front thickness (*thick line*) to increase. *B*, Predicted front width decreases but front velocity increases with increase in supersaturation. *C*, Increasing grain size from 0.01 to 1 mm causes an increase in front velocity (*thin line*) but a decrease in front width (*thick line*). *D*, Increase in input pH from 4 to 6 decreases both front velocity and front thickness.

graphic) and the macroscopic (paleomagnetic) evidence of isovolumetric replacement warranted adjusting reaction (3) for mineral volume. The field observation that the reaction front is narrow (fig. 2*a*) was introduced into the model (following Ortoleva et al. 1982, p. 625 ff., and Wang et al. 1995) by way of a self-consistent scaling of relevant variables—length, time, and aqueous concentrations—so that transport and reaction terms in the continuity equations are of the same order of magnitude. (If transport were slower than the mineral reactions at the front, these would stop; if transport were faster than the reactions, the front would be very wide.) The petrographic evidence of secondary porosity in the narrow leaching zone A of figures 2*a* and 2*c* confirms the prediction that the replacement, according to reaction (3), releases $H^+$ ions. The model incorporates—via $\beta_{calc} = 1$ (eq. [19])—the crucial condition that the calcite dissolution and secondary-porosity production in zone A must proceed at the same rate and at the same time as $H^+$ ions are released by the replacement (eq. [3]) in

zone B, despite the fact that the rate constant for calcite dissolution is orders of magnitude greater than the replacement rate.

The strategy of incorporating evidence of replacement and its kinetic and volumetric implications into the geochemical modeling of terra rossa genesis should be viewed not as circular but as necessary. If one looks again at figures 2*b*, 2*d*, and 2*e*, showing crinoid columnals in various stages of replacement—intermediate, incipient, and complete, respectively—one realizes that at all stages of replacement the kaolinite growth and the calcite dissolution must have been simultaneous and must have proceeded at the same rate, preserving mineral volume all along, an astonishing fact that the standard kinetic laws available would be unable to predict if we viewed replacement as resulting from just calcite dissolution and kaolinite precipitation, because the kinetic rate constant of calcite dissolution is many orders of magnitude greater than that for kaolinite growth. The equality of rates characteristic of any replacement, however, stops being a physicochemical conundrum if replacement is viewed as produced by guest-growth-driven pressure-solution of the host, a mechanism that has no trouble making the two rates mutually equal and preserving the solid volume, as demonstrated in figure 3, "Kinetics of the Kaolinite-for-Calcite Replacement," and references therein.

***Some Simplifying Assumptions.*** 1. To keep the number of components low, the several clay minerals that usually form terra rossa claystones are represented in the model by pure kaolinite. More realistic clay-mineral solid solutions are simulated in the numerical runs simply by adopting values of the equilibrium and rate constants higher than those for pure kaolinite.

2. The number of relevant aqueous species included in the model also was kept to a minimum (five) to minimize the number of mass conservation differential equations to be solved simultaneously. This, in effect, amounted to neglecting the species $AlOH^{2+}$ and $H_2CO_3$; thus, the model probably overestimates both the $H^+$ released by reaction (1) in the reaction zone and the secondary porosity, $\phi_\ell$, produced by that reaction (fig. 5*D*).

***Conclusions.*** 1. Quantitative reaction-transport simulations of the downward-advancing replacement of limestone by authigenic clays (represented by kaolinite) reproduce the formation of two adjacent subzones in the reaction front and the formation of considerable secondary porosity in subzone A, as observed. The moving secondary-porosity porosity wave, or soliton, predicted in figure 5*D* and confirmed by the occurrence of pores in the leaching zone (fig. 2*a*, 2*c*), may have a crucial role in triggering a reactive-infiltration instability that is probably responsible for producing the typical karst-sink morphology in the limestone that underlies terra rossa (Merino and Banerjee 2008).

2. Numerical simulations for moderate terra rossa porosity and for high values of the clay growth rate constant yield front widths of several centimeters, in good agreement with the observed thickness.

3. Similarly, model-predicted front velocities of several meters per million years agree well with two independent estimates of the rate of terra rossa formation, one derived from paleomagnetic measurements and the other derived from reasonable rates of eolian clay dust deposited at the land surface.

## ACKNOWLEDGMENTS

We thank M. Person of the New Mexico Institute of Mining and Technology for generous help and financial support to A. Banerjee; the Department of Geological Sciences at Indiana for support to A. Banerjee as an associate instructor; Y. Wang of Sandia Labs, Albuquerque, and R. T. Glassey of the Mathematics Department at Indiana University for advice at several stages of the modeling; J. Walther of Southern Methodist University for advice on the effects of solid solution on the kinetics of mineral reactions; S. Dworkin of Baylor University and X. Querol of the Spanish Research Council at Barcelona for references and data on dust deposition, chemistry, and mineralogy; J. Ganor of Ben Gurion University for help with deriving the half-life of eolian smectite particles at the earth's surface; and B. Wilkinson of Syracuse University and an anonymous reviewer for very helpful critical reviews of the manuscript.

## REFERENCES CITED

Aagaard, P., and Helgeson, H. C. 1982. Thermodynamic and kinetic constraints on reaction rates among minerals and aqueous solutions. I. Theoretical considerations. Am. J. Sci. 282:237–285.

Amram, K., and Ganor, J. 2005. The combined effect of pH and temperature on smectite dissolution rate under acidic conditions. Geochim. Cosmochim. Acta 69: 2535–2546.

Bowers, T. S.; Jackson, K. J.; and Helgeson, H. C. 1984. Equilibrium activity diagrams. New York, Springer, 397 p.

Busenberg, E., and Plummer, N. L. 1986. A comparative study of the dissolution and crystal growth kinetics of calcite and aragonite. *In* Mumpton, F. A., ed. Studies in diagenesis. U.S. Geol. Surv. Bull. 1578:139–168.

Carroll-Webb, S. A., and Walther, J. V. 1988. A surface complex reaction model for the pH-dependence of corundum and kaolinite dissolution rates. Geochim. Cosmochim. Acta 52:2609–2623.

Fletcher, R., and Merino, E. 2001. Mineral growth in rocks: kinetic-rheological models of replacement, vein formation, and syntectonic crystallization. Geochim. Cosmochim. Acta 65:3733–3748.

Ganor, J.; Mogollón, J. L.; and Lasaga, A. C. 1995. The effect of pH on kaolinite dissolution rates and on activation energy. Geochim. Cosmochim. Acta 59:1037–1052.

Kamb, W. B. 1961. The thermodynamic theory of nonhydrostatically stressed solids. J. Geophys. Res. 66: 259–271.

Meert, J. G.; Pruett, F.; and Merino, E. 2009. An "inverse conglomerate" paleomagnetic test and timing of in situ terra rossa formation at Bloomington, Indiana. J. Geol. 117:126–138.

Merino, E. 1975. Diagenesis in Tertiary sandstones from Kettleman North Dome, California. II. Interstitial solutions: distribution of aqueous species at l00°C and chemical relation to the diagenetic mineralogy. Geochim. Cosmochim. Acta 39:l629–l645.

Merino, E., and Banerjee, A. 2008. Terra rossa genesis, implications for karst, and eolian dust: a geodynamic thread. J. Geol. 116:62–75.

Merino, E., and Ransom, B. 1982. Free energies of formation of illite solid solutions and their compositional dependence. Clays Clay Miner. 30:29–39.

Metz, V., and Ganor, J. 2001. Stirring effect on kaolinite dissolution rate. Geochim. Cosmochim. Acta 65: 3475–3490.

Muller, J.-P.; Manceau, A.; Calas, G.; Allard, T.; Ildefonse, P.; and Hazemann, J.-L. 1995. Crystal chemistry of kaolinite and Fe-Mn oxides: relation with formation conditions of low temperature systems. Am. J. Sci. 295:1115–1155.

Nagy, K. L.; Blum, A. E.; and Lasaga, A. C. 1991. Dissolution and precipitation kinetics of kaolinite at 80°C and pH 3: the dependence on solution saturation state. Am. J. Sci. 291:649–686.

Nahon, D., and Merino, E. 1997. Pseudomorphic replacement in tropical weathering: evidence, geochemical consequences, and kinetic-rheological origin. Am. J. Sci. 297:393–417.

Ortoleva, P.; Merino, E.; Moore, C.; and Chadam, J. 1987. Geochemical self-organization I: reaction-transport feedbacks and modeling approach. Am. J. Sci. 287:979–1007.

Ortoleva P.; Merino, E.; and Strickholm, P. 1982. Kinetics of metamorphic layering in anisotropically stressed rocks. Am. J. Sci. 282:617–643.

Rabenhorst, M. C.; Wilding, L. P.; and Girdner, C. L. 1984. Airborne dusts in the Edwards Plateau region of Texas. Soil Sci. Soc. Am. J. 48:621–627.

Reheis, M., and Rademaekers, J. 1997. Predicted dust emission vs. measured dust deposition in the southwestern United States. *In* Impact of Climate Change and Land Use in the Southwestern United States. USGS Web workshop, http://geochange.er.usgs.gov/sw/.

Smith, R. M.; Twiss, P. C.; Kraus, R. K.; and Brown, M. J. 1970. Dust deposition in relation to site, season, and climatic variables. Soil Sci. Soc. Am. J. 34:112–117.

Vieillard, P. 2000. A new method for the prediction of Gibbs free energies of formation of hydrated clay minerals based on the electronegativity scale. Clays Clay Miner. 48:459–473.

Wang, Y.; Wang, Y.; and Merino, E. 1995. Dynamic weathering model: constraints required by coupled dissolution and replacement. Geochim. Cosmochim. Acta 59:1559–1570.

Wieland, E., and Stumm, W. 1992. Dissolution kinetics of kaolinite in acidic aqueous solutions at 25°C. Geochim. Cosmochim. Acta 56:3339–3355.